Baroclinic and barotropic tides in the Weddell Sea

ROBIN ROBERTSON

Lamont-Doherty Earth Observatory, Columbia University, Palisades, NY 10964, USA
rroberts@ldeo.columbia.edu

Abstract: Barotropic and baroclinic tides were simulated for the Weddell Sea using ROMS. The model estimates for both tidal elevations and velocities showed good agreement with existing observations. The rms differences were 9 cm for elevations and 1.2–1.7 cm s^{-1} for the major axes of the tidal ellipses for the semidiurnal constituents and 6–8 cm and 4.5 cm s^{-1} for the diurnal constituents, respectively. Most of the discrepancies occurred deep under the ice shelf for the semidiurnal tides and along the continental slope for the diurnal tides. Along the continental slope, the model overestimated the generation of diurnal continental shelf waves. The diurnal tides were barotropic throughout the basin. However, internal tides were generated at semidiurnal frequencies over rough topography. Over the continental slope, semidiurnal baroclinic tidal generation was enhanced by the existence of continental shelf waves, through their harmonics. Baroclinic tides generated over rough topography in the northern Weddell Sea incited inertial oscillations as they propagated south. These inertial oscillations varied with depth since they were incited at different depths at different times as the internal tide progressed. Both the baroclinic tides and inertial oscillations induced vertical shear in the water column and increased the divergence of the horizontal surface velocities.

Introduction

Much of the Antarctic Bottom Water (AABW) for the global ocean is formed in the Scotia Sea through the mixing of Weddell Sea Deep Water (WSDW) flowing out of the Weddell Sea (Fig. 1) with other waters (Deacon 1937). WSDW is formed in the Weddell Sea primarily through mixing of Warm Deep Water (WDW) either with Ice Shelf Water (ISW), which flows out of the Ronne–Filchner Ice Cavity or with shelf waters. Two shelf waters, High Salinity Shelf Water (HSSW) and Low Salinity Shelf Water (LSSW), exist in the Weddell Sea and they are formed on the continental shelves surrounding Antarctica through brine rejection associated with ice formation in the coastal polynyas.

Tides are a source of deep water mixing (Munk & Wunsch 1998, Garrett 2003) and are believed to be one of the sources of the mixing for WSDW formation. Tides influence mixing by increasing boundary layer shear and by induction of shear instabilities, which are associated with baroclinic tides. Tides also influence the circulation in the Weddell Sea through retardation of the mean flow due to their additional friction, induction of residual tidal velocities, and generation of continental shelf waves (CSW). These effects, in turn, affect the sea ice cover through increased divergence and convergence of surface velocities and their influence on the sea ice affects the ocean-atmosphere heat flux.

To evaluate the tidal effects, the tidal elevation and velocity fields must be known. Some tidal observations have been made in the Weddell Sea (Fig. 2) and a
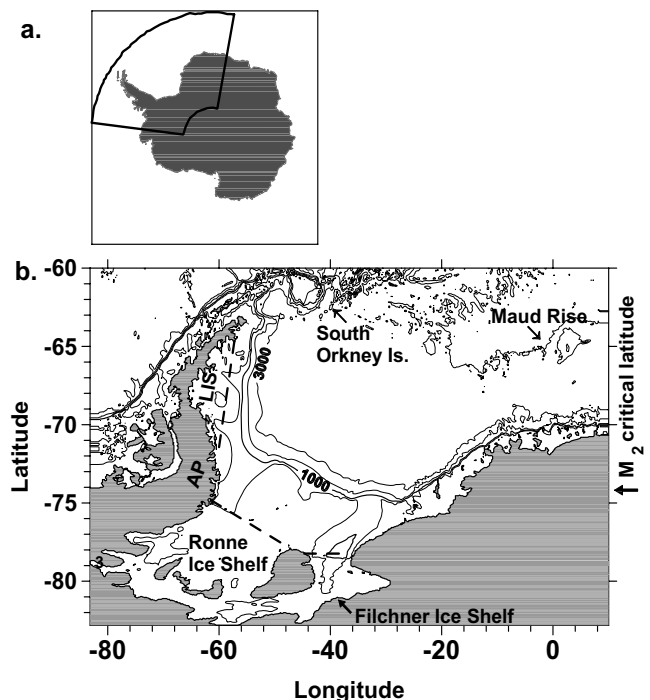

Fig. 1. a. The location of the model domain with respect to Antarctica. **b.** The model domain with the water column thickness contoured at 100, 500, 1000, 2000, 3000, and 5000 m. The Filchner–Ronne and Larsen Ice Shelf edges are indicated by dashed lines in b.
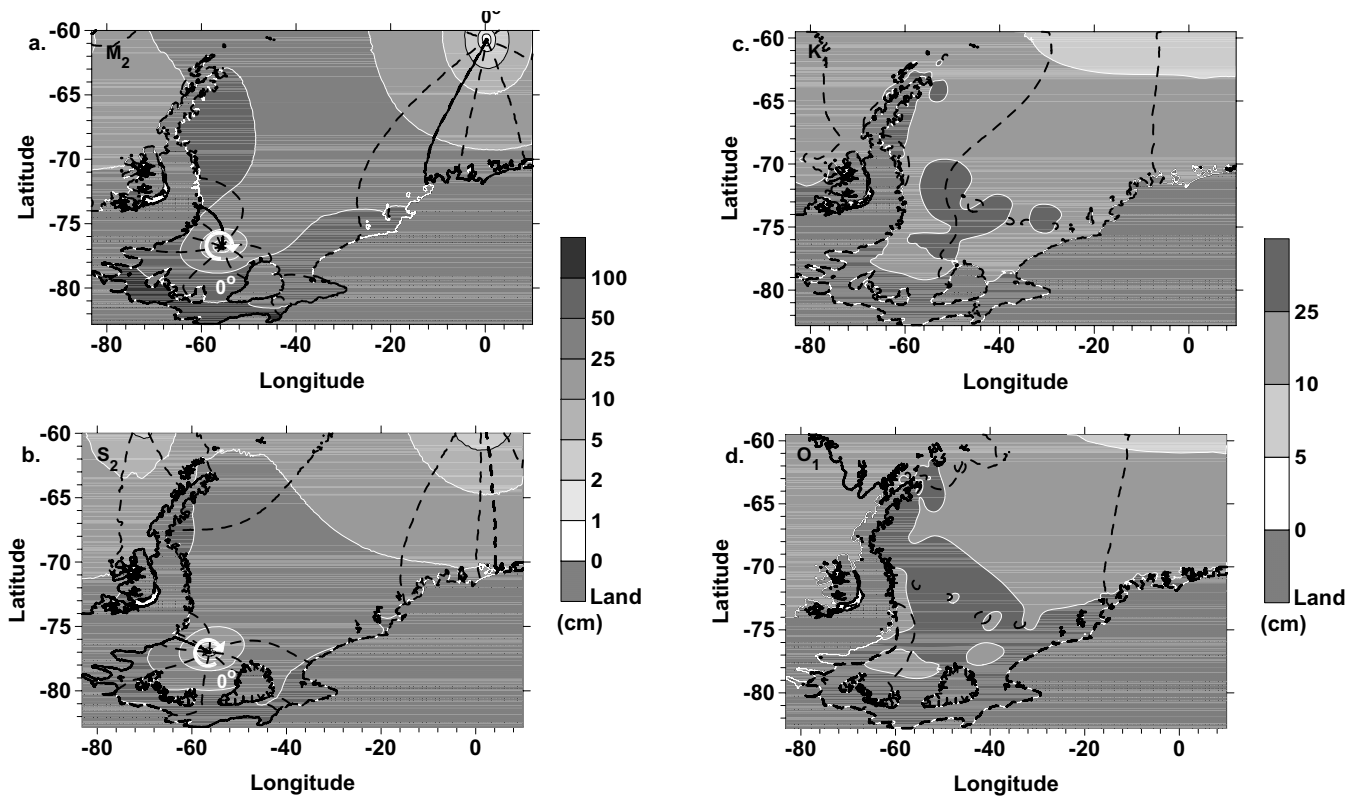
Fig. 2. The locations of tidal elevation observations are indicated by numbers in **a.** and those of velocity observations by numbers in **b.** The 500 m and 1000 m isobaths are shown. In **b.** three regions have been expanded in cutouts for legibility of the observation sites.

comprehensive list is given in Robertson *et al.* (1998). However, the observations are sparse and not well distributed within the basin, particularly the elevations (Fig. 2a). More complete coverage for the tidal fields can be provided through modelling. Smithson *et al.* (1996) modelled the barotropic tides for the region under the Filchner–Ronne Ice Shelf with reasonable agreement with

observations. Elevation and barotropic velocities for the entire Weddell Sea were generated by the two-dimensional tidal model of Robertson, Padman & Egbert for the four major constituents and the model estimates showed good agreement with observations (hereafter referred to as *RPE*) (Robertson *et al.* 1998). Further simulations with this model encompassed the circumpolar region, including both the

Fig. 3. The amplitude of the tidal elevation for the **a.** M_2, **b.** S_2, **c.** K_1, and **d.** O_1 constituents in cm. The overlaid heavy dashed lines indicate the phase lag for the elevation, with the zero phase lag line and direction indicated in **a.** and **b.**

Ross and Weddell seas. (CATS-99, CATS-2000, Laurie Padman unpublished). More recently, elevation information on portions of the Weddell Sea was provided by Padman *et al.* (2002) with their two-dimensional inverse model. However, no information on the vertical structure or the baroclinic tides was generated by these models. Baroclinic tidal information was provided along a two-dimensional transect over the continental shelf (Robertson 2001a, 2001b) and on an extremely coarse grid (Pereira *et al.* 2002), which had grid cells with widths in longitude ranging from 10–120 km. But the first model did not cover the entire Weddell Sea and the grid was too coarse in the longitude direction in the second model to resolve most of the baroclinic tides or continental shelf waves.

The goal of this project was to provide a description of the three-dimensional structure of the barotropic and baroclinic

tides for the entire Weddell Sea for the four major tidal constituents, M_2, S_2, K_1, and O_1. For this study, the Regional Ocean Modeling System (ROMS), described in the next section, was used.

Model description

The ROMS model in this application is fully described elsewhere (ROMS: Haidvogel *et al*. 1991, Song & Haidvogel 1993, 1994, Shchepetkin & McWilliams 2003) (this application: Robertson *et al*. 2003). ROMS had been modified previously to include the presence of a floating ice shelf (Robertson *et al.* 2003), including both mechanical and thermodynamic effects following Robertson (2001a) and Hellmer & Olbers (1989), respectively. Here only the pertinent details and recent modifications will be discussed.

Table I. Rms differences between the model estimates and observations for the elevation amplitude and phase lags for each constituent for the ROMS simulation and for the two-dimensional simulation of *RPE* (Robertson *et al*. 1998).

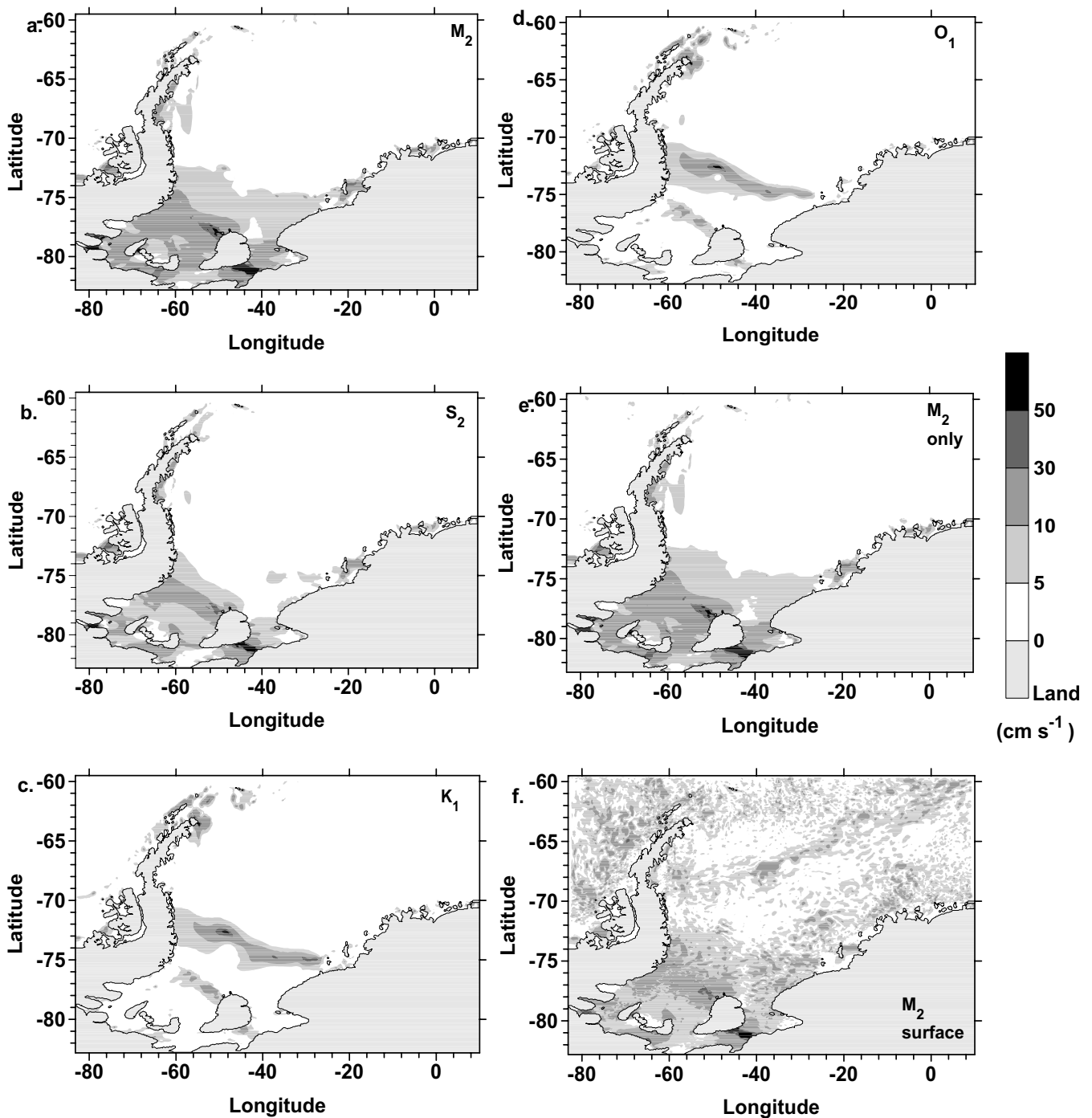| Constituent:		M_2		S_2		K_1		O_1	
		Amplitude (cm)	Phase Lag (°)	Amplitude (cm)	Phase Lag (°)	Amplitude (cm)	Phase Lag (°)	Amplitude (cm)	Phase Lag (°)
All Sites	ROMS	11.9	47	9.5	44	8.5	57	7.7	33
	RPE (1998)	8.9	38	7.1	45	8.0	58	7.4	29
Excluding Site 9	ROMS	8.5	48	8.6	44	8.4	50	5.6	33
	RPE (1998)	8.7	39	7.2	46	8.0	52	5.7	29

Fig. 4. The major axes of the tidal ellipses for the depth-independent velocities for the **a.** M_2, **b.** S_2, **c.** K_1, and **d.** O_1 constituents, in cm s^{-1}. **e.** The same for M_2 with only M_2 forcing, and **f.** for M_2 from the depth-dependent surface velocities.

Recently, improvements have been made in the vertical mixing parameterization for primitive equation models. Different vertical mixing parameterizations available in ROMS were evaluated using a sensitivity study at a site outside the study area with extensive hydrographic, velocity, and turbulence observations (Robertson, unpublished). For vertical mixing, the Generic Length Scale

(GLS) parameterization of Umlauf & Burchard (2003) was found to best replicate the observed velocities and vertical diffusivities (Robertson, unpublished) The GLS scheme was used for these simulations. Tidal forcing was implemented by setting elevations along all the open boundaries, with the coefficents taken from a global, two-dimensional inverse model (TPXO6.2 Egbert & Erofeeva

2002). Four major tidal constituents were used, two semi-diurnals, M_2 and S_2 and two diurnals, K_1 and O_1.

The model domain (Fig. 1) covered the Weddell Sea with a grid spacing of 0.045° in latitude, 0.186° in longitude, and 24 vertical levels. The ice thickness and water column thickness, defined as the distance between the bottom and the ice shelf base (or ocean surface), were taken from BEDMAP (Lythe *et al.* 2000). In the northern region beyond the extent of BEDMAP, the water column thickness was taken fromSmith & Sandwell (1997). No smoothing was performed on either the water column or the ice shelf thicknesses. The minimum water column thickness was set to 30 m, which entailed artificially deepening a small portion of the region under the ice shelf, particularly near the eastern grounding line. The barotropic and baroclinic mode time steps were 6 s and 180 s, respectively, and the simulations were run for 30 days, with hourly data from the last 15 days saved for analysis. The kinetic and potential energies stabilized after around 15 days, thus the first 15 days of simulated data was discarded.

Initial potential temperature, θ, and salinity, S, fields were assembled from the World Ocean Circulation Experiment (WOCE) Hydrographic Programme Special Analysis Center (Gouretski & Janke 1999), except under the ice shelf. Here, the hydrography was essentially a four layer system based on a θ and S profile through the ice shelf at a single location (90/2 (site 1 in Fig. 2b)) (Robinson & Makinson 1992), in a similar manner as was done for the Ross Sea (Robertson 2005). The model elevation and velocities were initialized with the geostrophic velocities associated with the initial hydrography as determined from a simulation without tidal forcing.

Elevation, η, and depth-independent velocities, U_2 and V_2, are produced by the two-dimensional (barotropic) mode of the model and θ, S, and depth-dependent velocities, U_3, V_3, and W_3, by the three-dimensional (baroclinic) mode. The depth-dependent velocities fully represent the velocity at each grid cell and do not have the depth-independent velocity removed. Foreman's tidal analysis routines were used to analyse these fields (Foreman 1977, 1978).

Results

Elevations and depth-independent velocities

Semidiurnal constituents (M_2 and S_2)
The semidiurnal tides propagated westwards around the Antarctic continent, splitting into two portions at the continental slope ~30°W, with one portion following the continental slope and the other following the Antarctic continent under the Ronne–Filchner Ice Shelves. Two amphidromic points were formed for the semidiurnal constituents, one at ~ 0°W and one at the edge of the Ronne Ice Shelf, ~ 56°W (Fig. 3a & b). These results are consistent with those of a barotropic model (*RPE*) (Robertson *et al.* 1998).

In order to evaluate the performance of the model, the elevation amplitudes and phase lags were compared to existing elevation observations for the region, using the twenty-four locations shown in Fig. 2a. The observations and their sources are discussed in Robertson *et al.* (1998) and a good summary is given in Smithson *et al.* (1996). It should be noted that sites 1–3, 5, and 9 were collected on the ice shelf using tilt meters, which have been shown to have errors (Doake 1992). Thirteen of the twenty-four estimates for the M_2 constituent and 13 of the 22 estimates for the S_2 constituent fell within the observational uncertainties. The model generally underestimated the tidal amplitudes along the continental slope and at a site under the western portion of the Ronne Ice Shelf (site 9) for both semidiurnal constituents. The model phase lag estimates fell outside the uncertainties at five sites for each semidiurnal constituent. Most of the phase lag discrepancies occur in the ice shelf cavity in the vicinity of the amphidromic point, where small errors in the location of the amphidromic point result in large phase lag errors. The performance was similar to that of *RPE*, with rms errors for the M_2 and S_2 elevation amplitudes and phase lags were 11.9 cm and 47° and 9.5 cm and 44°, respectively (Table I). These are slightly larger than those of *RPE*, 8.9 cm and 38° for M_2, and 7.1 cm and 45° for S_2, respectively. For both models, much of the rms error was associated with site 9. Site 9 had a short record length, 9 days, and the observation is suspect. When site 9 was excluded, the rms errors were reduced to 8.5 and 8.6 cm for ROMS and 8.7 and 7.6 cm for *RPE* (Table I). The two models agreed well, particularly considering differences in the boundary forcing, topography and hydrography and the two-dimensional dynamics of RPE versus the three-dimensional dynamics of ROMS.

The depth-independent velocities for the semidiurnal constituents are small, < 5 m s^{-1}, in the deep basin, increasing over the continental slope and under the ice shelves (Fig. 4a & b). Major axes > 10 cm s^{-1} are reached under the Ronne–Filchner Ice Shelf for M_2 and at the front of the Ronne–Filchner Ice Shelf for S_2 and at the grounding line of the Larsen Ice Shelf and between some of the islands along the south-eastern coast for both (Fig. 4a & b). Again the topography was the primary controlling factor for the depth-independent velocities, as has been previously noted for *RPE* and in the Ross Sea (Robertson 2005).

A slight increase in the semidiurnal major axes occurs due to continental shelf waves (CSWs). This can be seen by the small regions with larger major axes, > 10 cm s^{-1}, along the continental slope in Fig. 4a & b, which are present when four tidal constituents were used for forcing. These regions are not present or are diminished when forced by only the semidiurnal constituent M_2 (Fig. 4e). At the shelf break, the diurnal constituents excite CSWs along the continental slope where WDW and shelf waters meet. Since the semidiurnal constituent frequencies are at or near the first harmonic of the diurnal constituents, interactions between
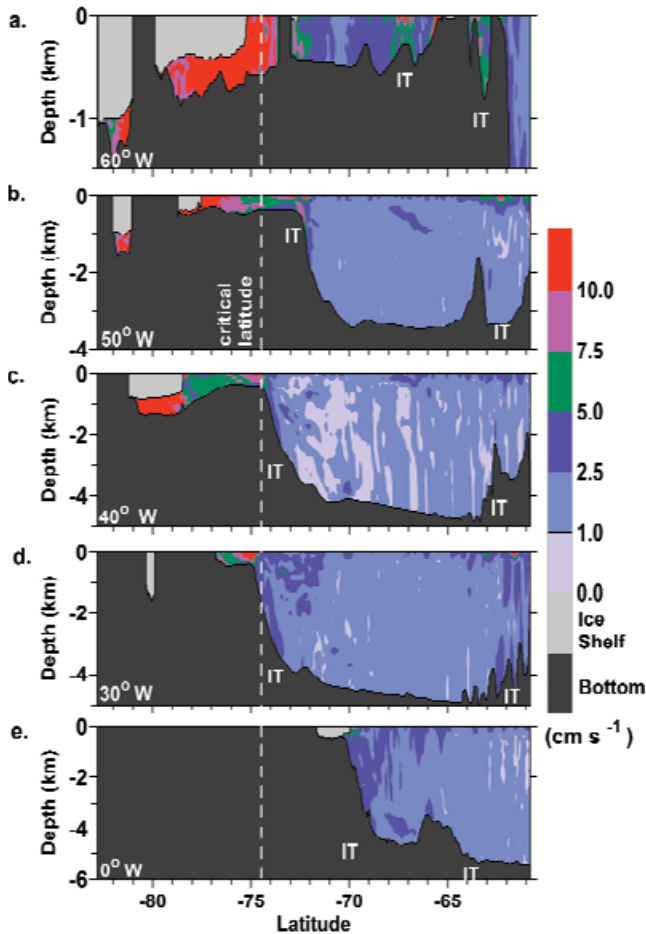
Fig. 5. The major axes of the M_2 tidal ellipses from the depth-dependent velocities along N–S transects at **a.** 60°W, **b.** 50°W, **c.** 40°W, **d.** 30°W, and **e.** 0°W. IT indicates locations of internal tidal generation. The location of the critical latitude is indicated by a dashed line.

the CSW and variations in topography transfer energy from the diurnal tides to their first harmonic, which is interpreted as semidiurnal tides in the analysis. The mechanism for the transfer is related to the harmonics, with the diurnal CSWs modulating the hydrography through the position of the front between the WDW and shelf waters at roughly twice the inertial frequency and the semidiurnal tides picking up the energy at near inertial frequencies, since along the continental slope in the southern Weddell Sea, the inertial frequency is near the semidiurnal tidal frequency. The influence of the CSWs on the semidiurnal depth-independent velocities was also noted in the Ross Sea (Robertson 2005).

Diurnal constituents (K_1 and O_1)

The diurnal tides also propagated as a Kelvin wave westwards through the basin, but they did not split like the semidiurnal constituents and amphidromic points are not formed (Fig. 3c & d). Along the continental slope,
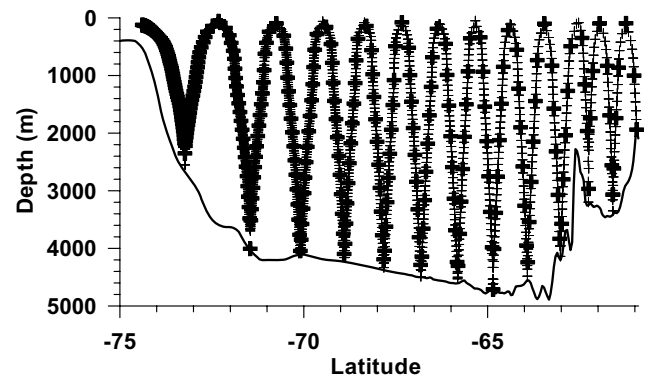

Fig. 6. Internal wave ray characteristics starting from 60°57'S and propagating south for the hydrography and topography used in the model along 40°W according to linear internal wave theory without dissipation. The bold crosses are separated by one M_2 tidal period.

Continental Shelf Waves (CSW) are formed by both diurnal constituents resulting in patches of higher and lower elevation amplitudes and changes in the phase lag (Fig. 3c & d). The model estimates showed reasonable agreement with the observations with rms differences of 8.4 cm and 50° for K_1 and 5.6 cm and 33° for O_1 when site 9 is excluded (Table I). Most of the discrepancies occur along the continental slope where the CSWs are generated. And again, the model performance was equivalent to that of *RPE*.

CSWs are excited by interactions of currents with topographic irregularities. Excellent summaries of their properties are given by Huthnance (1978) and Brink (1991). They are coastally trapped waves with sub-inertial frequencies. In the Weddell Sea, CSWs are excited by the diurnal tides, but not the semi-diurnal tides. In the southern hemisphere, CSWs phase propagates westwards, while the group velocity (energy) propagates eastwards (Huthnance 1978, Middleton *et al*. 1982, Brink 1991). In weak stratification, they are essentially barotropic. Increasing stratification will increase the wave speed and induce the frequency to increase. The CSWs decay primarily through friction. Realistic topography was found to concentrate the motion over the upper slope and shelf. In the presence of mean alongshore flow, the properties of CSWs change due to a combination of Doppler shift, changes in the background vorticity, and the growth of instabilities. The behaviour of the mode one CSWs present in the model results is consistent with this theoretical behaviour, with a westward propagation and a concentration of motion over the upper slope and shelf. The CSWs appear to be tied to specific topography.

The major axes of the tidal ellipses for the diurnal constituents were less than 10 cm s^{-1} except along the continental slope, along the Ronne Ice Shelf edge, and near the South Orkney Islands and the tip of the Antarctic Peninsula (Fig. 4c & d). The larger velocities along the continental slope and the ice shelf edge are clearly
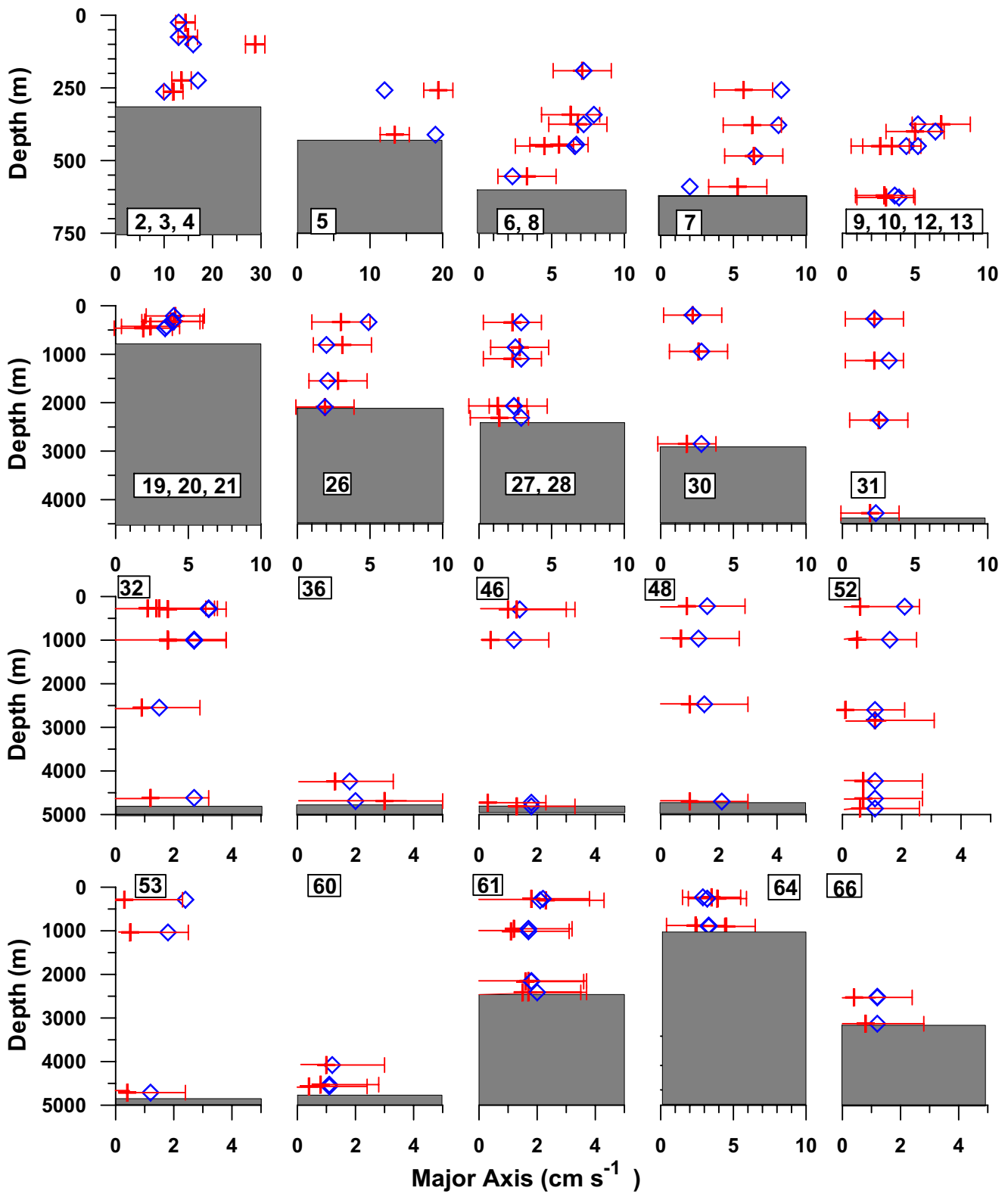
Fig. 7. Major axes of the M_2 tidal ellipses from ROMS (blue diamonds) compared against observational data (red crosses). The error bars indicate the observational uncertainty (1.7 cm s^{-1}). The top row shows locations near the ice shelf edge. The second row shows locations along the eastern end of the transect across the Weddell Sea and the third and bottom rows for the deep, middle section and the western end, respectively. The observation site numbers are indicated for each panel in the boxes and the observed water depth is indicated by the shaded box.

Table II. Rms differences for the major axes of the tidal ellipses and absolute errors for the positive and negative rotating components from the depth-dependent velocities at the observation locations for each constituent from ROMS.

| | | All observations | | | |
		M_2	S_2	K_1	O_1
Rms		1.7	1.2	4.5	4.5
Positive rotating component (anticlockwise)	Absolute error	1.23	0.91	1.76	1.58
Negative rotating component (clockwise)	Absolute error	1.01	0.69	0.87	0.89
No. of sites exceeding uncertainty		9	7	26	27

associated with CSW. The amplified response at the other locations is likely to be local CSWs, as has been observed at locations such as Fieberling Guyot (Brink 1991).

Depth-dependent response

Semidiurnal constituents (M_2 and S_2)
Internal tides were generated over regions of steep topography, particularly along the continental shelf/slope break in the south and over the complex topography in the north. This is apparent by the vertical variation in the major axes for the depth-dependent velocities along longitude transects (indicated by IT in Fig. 5). The locations of internal tide generation match those predicted by linear internal wave theory using Baines criteria (Baines 1974) (not shown). As predicted by linear internal wave theory, significant generation of M_2 tides occurred in two regions: over the continental slope and over the rough topography in the northern Weddell Sea. The continental slope in the southern Weddell Sea is near the M_2 critical latitude, 74°28.8'S (Fig. 1b and dashed line in Fig. 5). At the critical latitude the inertial frequency equals the tidal frequency, which affects both the generation and propagation of internal tides. Linear internal wave theory predicts that internal waves will not be generated nor propagate poleward of the critical latitude (A more extensive explanation of the relevant linear internal wave theory is given in Robertson (2001a).) The internal tides had wavelengths (~60–80 km) and propagated along internal wave rays in accordance to linear theory with shallower slopes for the wave ray characteristics nearer to the critical latitude and steeper slopes more distant from it. An example of internal wave rays for the region is shown in Fig. 6.

Some amplification of semidiurnal internal tide generation occurred where CSWs were generated, which did not occur when the model was forced with M_2 only (not shown). In the Weddell Sea, the continental slope is near the M_2 critical latitude and is the location for CSW generation and propagation. The CSWs modulate the stratification, the position of the WDW and shelf waters and the front between them. These density changes affect both internal

tide generation and propagation and cause energy to be transferred from the diurnal frequencies, which are roughly twice the inertial frequency to the semidiurnal frequencies, which are roughly equal to the inertial frequency, particularly M_2.

The propagation for the two primary regions of baroclinic tidal generation was quite different. Baroclinic tides propagated along wave characteristics, an example of which is shown in Fig. 6 for a mode one M_2 internal wave originating at 60°57'S and travelling south along a north–south transect at 40°W. Of course, the internal waves do not always propagate directly south, so Fig. 6 shows just a subset of the propagation. However, it shows several key elements of baroclinic propagation according to linear internal wave theory. First, wave rays are more horizontal in the upper ocean where the density gradients are stronger and more vertical in the deeper ocean and the mixed layer where the density gradients are weaker. Near the critical latitude, the internal wave rays flatten out and become more
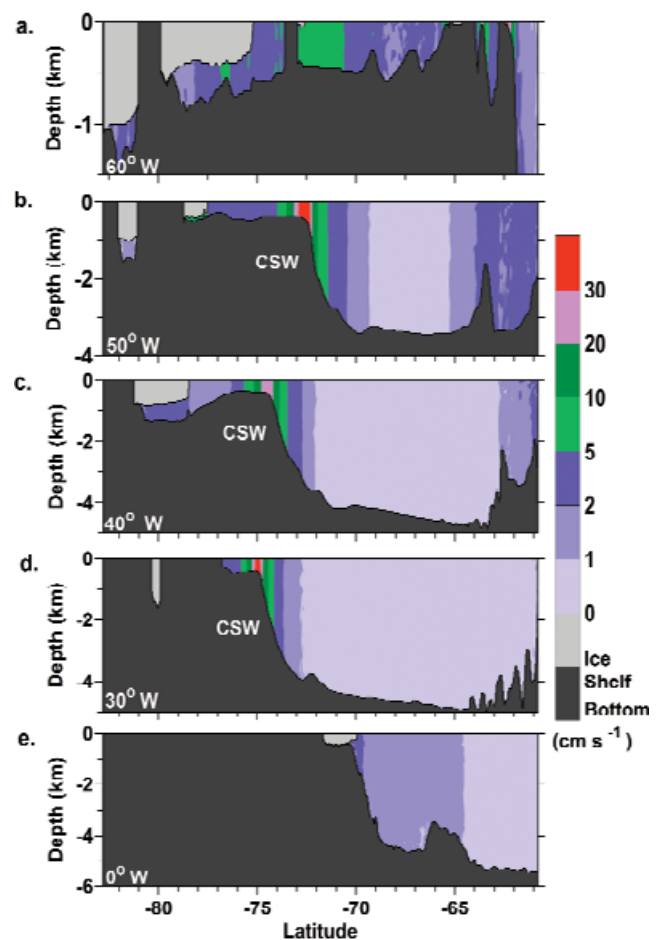

Fig. 8. The major axes of the K_1 tidal ellipses from the depth-dependent velocities along N–S transects at **a.** 60°W, **b.** 50°W, **c.** 40°W, **d.** 30°W, and **e.** 0°W, in cm s^{-1}. CSW indicates continental shelf waves.
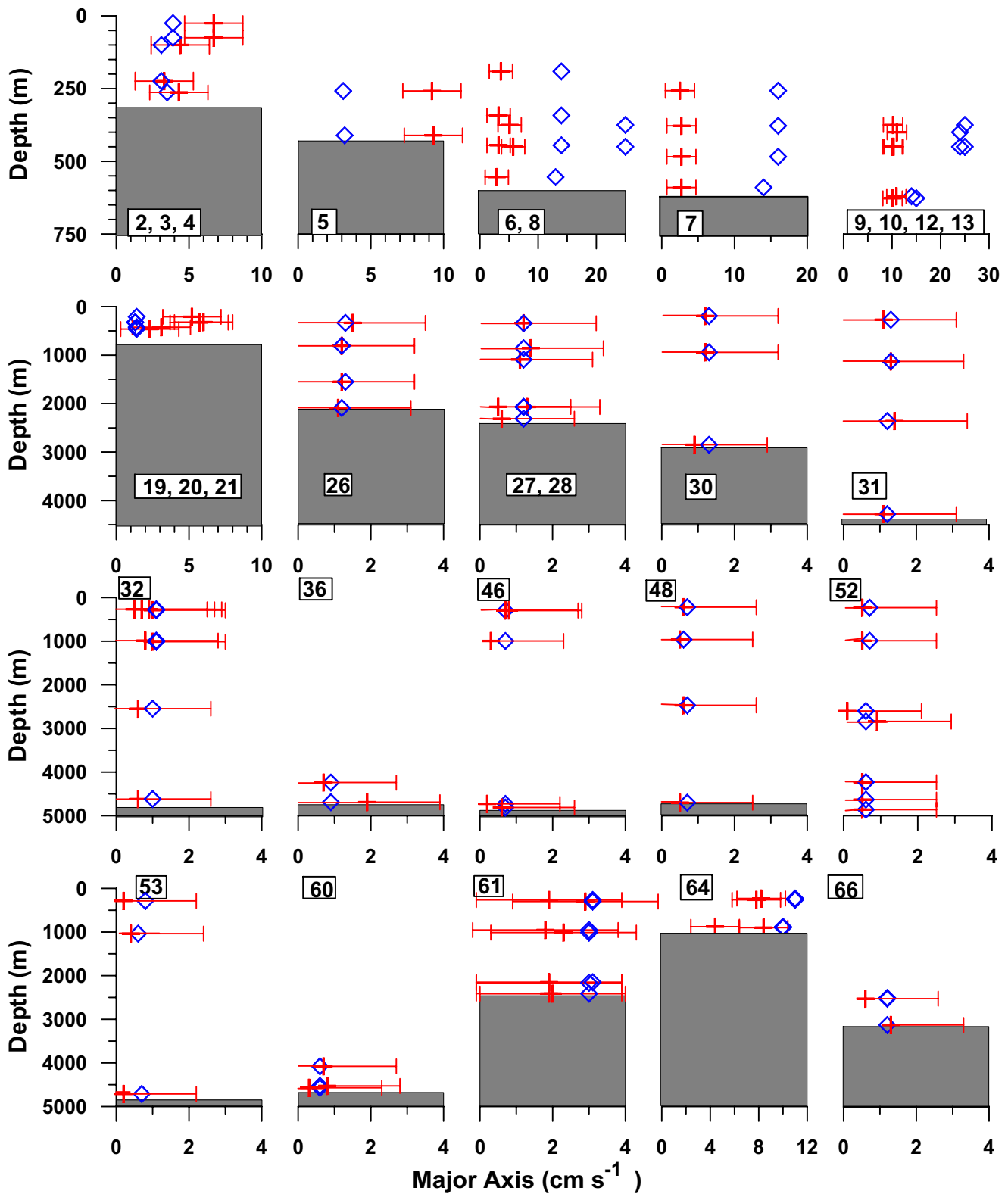
Fig. 9. Major axes of the K_1 tidal ellipses from ROMS (blue diamonds) compared against observational data (red crosses). The error bars indicate the observational uncertainty (1.7 cm s^{-1}). The top row shows locations near the ice shelf edge. The second row shows locations along the eastern end of the transect across the Weddell Sea and the third and bottom rows for the deep, middle section and the western end, respectively. The observation site numbers are indicated for each panel in the boxes and the observed water depth is indicated by the shaded box.
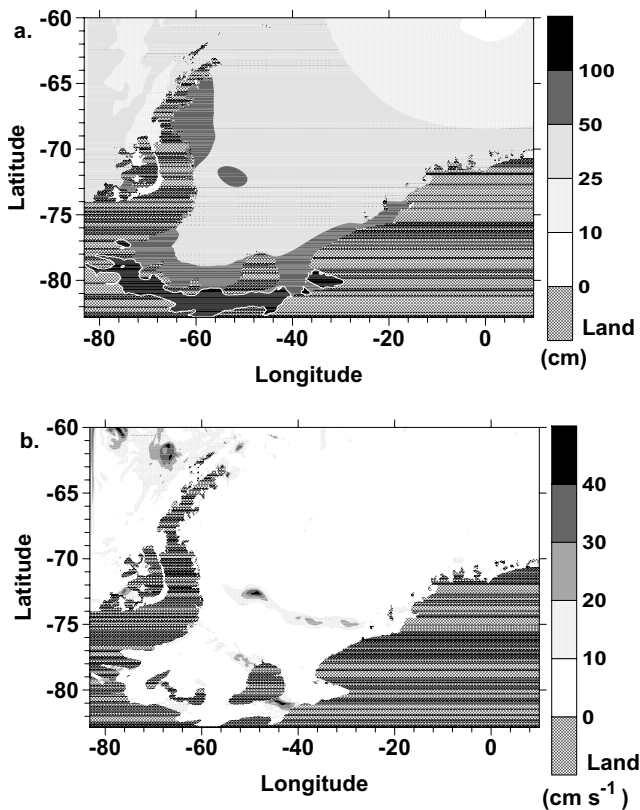
Fig. 10. a. The standard deviation of the elevations (cm), and **b.** the combined standard deviations of the depth-dependent surface velocities (cm s^{-1}).

Fig. 11. The combined standard deviations in the depth-dependent velocity anomalies (difference between the depth-dependent and depth-independent velocities) over 15 days at **a.** 60°W, **b.** 50°W, **c.** 40°W, **d.** 30°W, and **e.** 0°W. The M$_2$ critical latitude is indicated by a dashed white line.

horizontal. Also propagation for M$_2$ stops at its critical latitude. The crosses are equally spaced with the bold crosses separated roughly by one tidal period. The group speed is smaller nearer to the critical latitude, as seen by the closeness of the crosses. Baroclinic tides generated along the continental slope in the southern region propagate primarily northward since they are prevented from propagating south by the critical latitude (Figs 5 & 6). With the slower group speed, internal tides generated in the south do not propagate as far as those generated in the north, with larger group speeds. When the continental slope is more than a degree north of critical latitude (Fig. 5b), a portion of the baroclinic tide propagated south until it was turned by the critical latitude. In the northern region, the baroclinic tides propagated both north and south, but the northward propagating waves were either reflected by the high ridge or quickly left the domain (Fig. 5).

To evaluate the performance of the model, the model estimates were compared to 143 velocity observations from 68 mooring sites (Fig. 2b). Most of this data is discussed fully in Robertson *et al.* (1998), although data from recent programs has been added: CORC/Arches (Visbeck, personal communication 2003) and Ropex (Nicholls, personal communication 1999). Generally, the model estimates were slightly higher than the observations, but
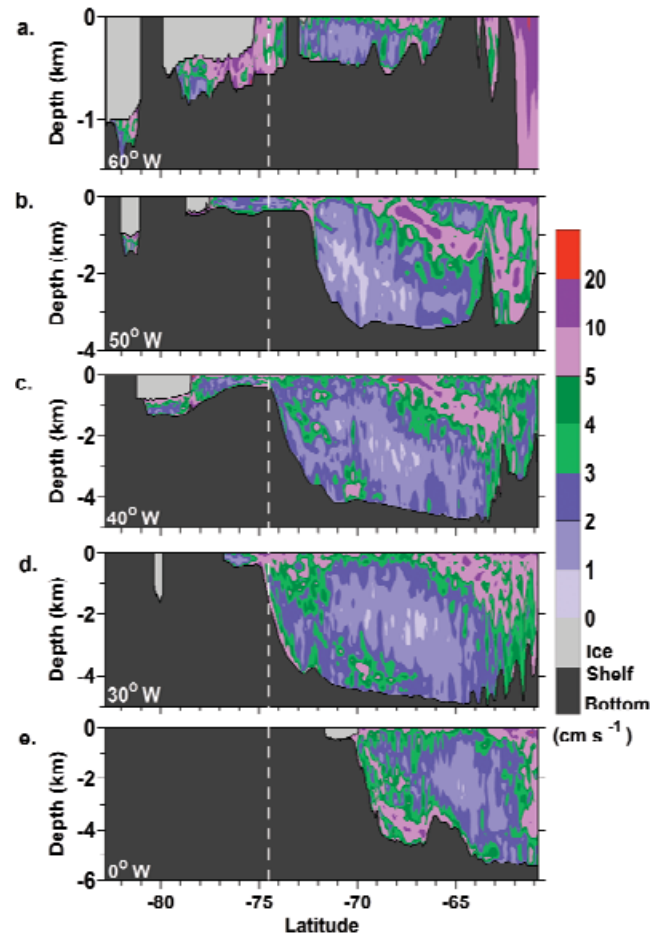
within the observational uncertainties (Fig. 7). The model reproduced much of the vertical structure of the observations for M$_2$ as seen in comparisons of the model estimates (diamonds) and the observations (crosses) (Fig. 7). Figure 7 includes most of the mooring sites with multiple measurements, with nearby multiple mooring sites often shown together. The good agreement between the model estimates and observations is reflected in the low rms differences for the major axes: 1.7 cm s^{-1} and 1.2 cm s^{-1} for the M$_2$ and S$_2$ constituents, respectively.

The rms difference reflects only the errors in the major axes. A more comprehensive measure is the absolute error, which combines errors in the amplitude with those in phase. The absolute errors (E_A) for each constituent were calculated for both positive (anticlockwise) and negative (clockwise) components according to
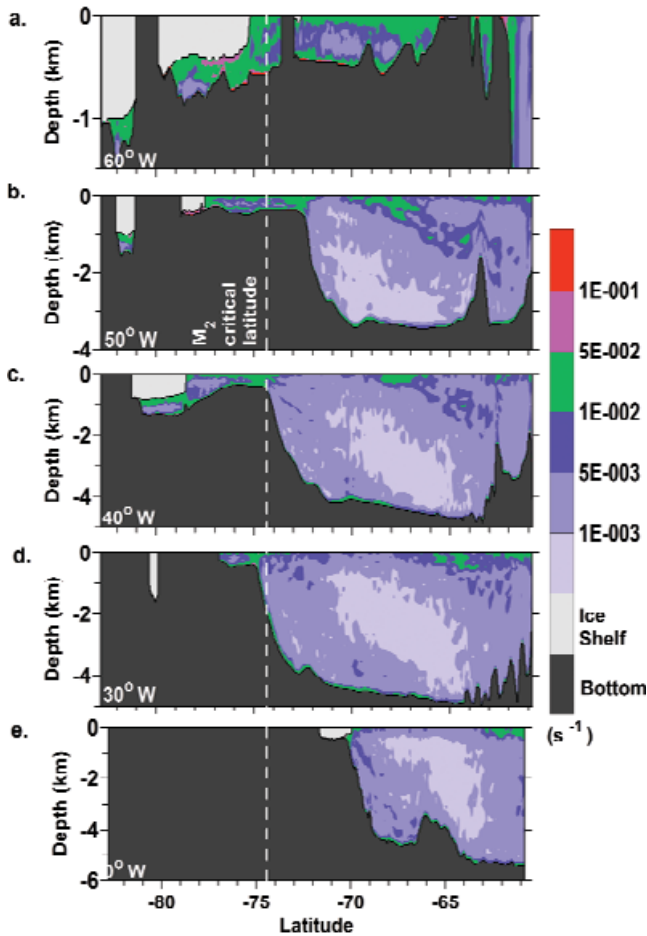
$$E_A = L^{-1} \sum_L D,$$

with,

Fig. 12. Vertical shear in the depth-dependent velocities along N–S transects at **a.** 60°W, **b.** 50°W, **c.** 40°W, **d.** 30°W, and **e.** 0°W. The M$_2$ critical latitude is indicated by a dashed white line.

$$D = \sqrt{0.5\left(A_o^2 + A_m^2\right) - A_o\, A_m \cos\left(\varphi_o - \varphi_m\right)},$$

where L is the number of observations and A_o and A_m and φ_o and φ_m are the amplitudes and phase lags, respectively, with the subscripts of o and m representing the observations and model results, respectively (Cummins & Oey 1997). The absolute error is determined for each component for each constituent. The absolute errors in the positive components for M$_2$ and S$_2$ were 1.2 and 0.9 cm s^{-1} respectively (Table II). In the Southern Hemisphere, most of the baroclinic response for the boundary layers should be associated with the positive rotating component. The negative rotating component is associated with the barotropic response in the Southern Hemisphere. The absolute errors in the negative components for M$_2$ and S$_2$ were smaller, 1.0 and 0.7 cm s^{-1}, respectively (Table II). The larger absolute errors for the positive rotating component indicate that more error is associated with the baroclinic response than the barotropic response.

Most of the locations where the model exceeded the observational uncertainties (sites 2, 5, 7, 8, 10, and 53) were along the ice shelf edge (sites 2–5) or along the continental slope (sites 7–14). There are several sources for the differences between the model estimates and the observations, but the primary ones are topography and observational errors. Even more than elevations, the velocities are very sensitive to topography and errors in the topography will result in errors in the velocity estimates. Neither the water depth nor the ice shelf draft are well known, leading to errors in the topography and, in turn, the model estimates. The ice shelf is also assumed to float, which is true at its front. However, between the grounding line and the hinge line, the ice shelf does not float and the model does not include the proper dynamics for the grounded ice shelf. Additionally, the observed water depths at the observation locations were often different than that used by the model. Many of the velocity measurements were taken in the benthic boundary layer. If the model bathymetry for a location has a different water depth than that used by the model, the model estimate at the corresponding depth will not be at the corresponding location with respect to the bottom and the boundary layer resulting in a difference. For example the deepest values at site 7 is in the boundary layer for the model but not the observation (Fig. 7) and the deepest values at sites 8 and 10 are in the boundary layer for the observation, but not the model. Observational errors exist and differences occur between observations at nearby locations for example at site 28 the observations at the depths 2066 m and 2069 m differ by more than a factor of two. The same occurs for repeat measurements, for example site 32. Additionally for the instruments located near the critical latitude, observations may be contaminated by inertial oscillations, which are impossible to separate from the semidiurnal frequencies at these latitudes, especially for short records.

With the exception of the aforementioned mismatches, the model replicates the vertical structure of the internal tides reasonably well in the various regions of generation: along the front of the Ronne Ice Shelf (sites 2–4 in Fig. 7), along the continental slope (sites 6–13 in Fig. 7), along the eastern continental shelf (sites 19–21, 26–28, 30–31 in Fig. 7), over Maud Rise (site 48 in Fig. 7) and over the rough topography of the northern Weddell Sea (sites 52 and 61 in Fig. 7). Under the ice shelf at sites 2 and 5, the model underestimated the velocity in the upper layer and overestimated the velocity in the lower layer. This is probably related to the simplified hydrography used under the ice shelf. Unfortunately, the observational data is too sparse and the coverage is too incomplete to provide a robust verification of the model.

Baroclinic velocities are important to the divergence of the surface velocities, which induce lead formation in the pack ice. This has been observed by Geiger *et al.* (1998). The baroclinic velocities introduce additional divergence at the surface (Fig. 4e) compared to the depth-independent velocities (Fig. 4a). Since surface velocity divergence

affects lead formation in this region, the internal tides will generate more lead formation than that due to the barotropic tide alone.

Diurnal constituents (K_1 and O_1)

The diurnal tides behaved barotropically, with only slight depth dependence (Fig. 8). This is the expected behaviour for this region, since it is far poleward of the diurnal critical latitudes (28° and 30°) and internal tide generation is not expected at their frequencies. Most of the depth-dependence was a boundary layer response (Fig. 8). The slight mid-water column depth-dependence, which does occur outside the benthic boundary layer, coincides with locations of semi-diurnal internal tides.

The diurnal major axes were larger than those of the semidiurnal constituents, reaching 50 cm s^{-1} compared to 10 cm s^{-1}. The largest major axes and most greater than 10 cm s^{-1} were associated with diurnal CSWs over the continental shelf break near 73–75°S (denoted by CSW in Fig. 8).

The performance of the model in replicating the observations for the diurnal constituents was also evaluated (Fig. 9). Generally, the model estimates for the depth-dependent major axes fell within the observational uncertainty, except for sites 2, 3, 5–14, 19, 21, 22, and 64. Most of the disagreement sites occurred along the continental slope (sites 6–14, 19–30) (Fig. 9) where the model overestimated the generation of CSWs. Overestimation of CSWs also occurred in the Ross Sea (Robertson 2005) and with *RPE*. There was also disagreement at several sites along the ice shelf front (sites 2, 3, and 5) where the model underestimated the velocities. A similar situation occurred for the diurnal tides in the Ross Sea (Robertson 2005). Rms differences between the model estimates and observations were 4.5 cm s^{-1} for K_1 and O_1 (Table II). Absolute errors in the positive rotating component were 1.8 and 1.6 cm s^{-1} for K_1 and O_1, respectively and ~0.9 cm s^{-1} for the negative rotating component for both diurnal constituents (Table II).

Combined tidal response

So far, the discussion has focused on the model performance and the individual constituents. Most of the tidal influence on the pack ice, sediments, mixing, etc. occurs due to the combined elevation and/or velocities. To evaluate the combined tidal response, standard deviations were calculated for the surface elevations and both depth-independent and depth-dependent velocities. Standard deviations for the elevations exceeding 50 cm occurred under most of the ice shelves, including those west of 16°W (Fig. 10a). Standard deviations greater than 50 cm also occurred over a region along the continental slope at ~52°W as a result of CSWs (Fig. 10a). At the grounding line of the Filchner–Ronne Ice Shelf, standard deviations were typically 1.0 m and reached 2.0 m at some locations near the

grounding line (Fig. 10a). Since the model assumes the ice shelf is floating, and in actuality the ice shelf is grounded at the continental edge and does not move, these high standard deviations are likely to be overestimates.

High standard deviations, > 10 cm s^{-1}, in the depth-dependent surface velocities occurred along the continental slope where CSWs were generated, along the Ronne Ice Shelf edge, under the Filchner Ice Shelf, and north-west of the Antarctic Peninsula in an area of rapidly changing topography (Fig. 10b). The high standard deviations along the continental slope and ice shelf edge result from CSW. The rough topography north of the Antarctic Peninsula generates internal tides in that region.

In the depth-dependent velocity transects (Fig. 11), the standard deviations of the velocity anomalies, defined as the difference between the depth-dependent and depth-independent velocities, were also high at the surface for these locations. But in addition, high standard deviations occurred within the water column coinciding with steep topography and the generation of internal tides. There are three prominent locations of mid-water column high standard deviations: along front of the ice shelves, along the continental slope, and south of the rough topography in the northern Weddell Sea. As seen in Fig. 5, baroclinic tides are generated in these three regions. However, spectral analysis showed that much of the energy for the high standard deviations north of 70°S did not occur at a tidal frequency, but at or near the inertial frequency. Baroclinic tides propagating south along the internal wave ray characteristics (a typical example is shown in Fig. 6) induced inertial oscillations as they propagated. These inertial oscillations had a depth dependency since they were induced at different depths at different times during propagation. In the pycnocline, stronger inertial oscillations were induced, however, there are no observations to confirm the existence and strength of these inertial oscillations.

Vertical shears of the horizontal velocities are important since they have the potential to induce mixing in the water column in certain stratification conditions through the development of shear instabilities. The primary sources of vertical shear in the horizontal velocities were depth-varying inertial oscillations, boundary layers, and mid-water column baroclinic tides (Fig. 12). Both the benthic boundary layer and the surface boundary layer under the ice are apparent in the shear estimates (Fig. 12). Additionally, high mid-water column vertical shears coincide with the locations of internal tides (Fig. 12) and the depth-varying inertial oscillations (Fig. 11). Mid-water column vertical shears exceeding 1 x 10^{-3} s^{-1} occurred along the continental slope where the CSW enhanced internal tide generation and under the ice (Fig. 12). Estimates of the Richardson number by the model indicated an unstable water column in some of these regions (not shown).

Summary

Simulations of the barotropic and baroclinic tides in the Weddell Sea basin and the cavity under the Filchner–Ronne and Larsen Ice Shelves were performed with combined forcing of four tidal constituents, M_2, S_2, K_1, and O_1, using ROMS. Comparison of the model results with tidal estimates showed good agreement for elevations for all constituents and for velocity estimates for the semidiurnal constituents, M_2 and S_2. The agreements for velocity for the diurnal constituents, K_1 and O_1, were not as good, particularly along the continental slope, where the model overestimated the tidal response in the form of continental shelf waves.

The diurnal tides were essentially barotropic with vertical differences in their response associated with the benthic and surface boundary layers. The baroclinic response occurred at the semidiurnal frequencies. Semidiurnal baroclinic tides were generated along the continental shelf break and over regions of steep topography. The baroclinic tidal behaviour was consistent with that for internal waves in a continuously stratified fluid and propagating along wave rays with wavelengths corresponding to the theoretical estimates for mode one internal waves. The semidiurnal baroclinic tides were significantly amplified by the diurnal continental shelf waves where they were present. The semidiurnal tides were found to induce inertial oscillations in the northern Weddell Sea. These inertial oscillations varied with depth, since they were incited at progressively later times at different depths as they propagated through the water column.

Although the agreement between the model estimates and observations is good, the sparseness of the dataset is insufficient to provide a definitive verification that the model is replicating the conditions in the Weddell Sea. Nevertheless, there is room for improvement in the model predictions. The model estimates will improve as knowledge of topography and bathymetry improves. The German ISPOL project is obtaining hydrographic and bathymetric data for the seldom visited western Weddell Sea and the velocity data will be available for tidal analysis (H. Hellmer, personal communication 2004). Data from this sources will be incorporated into the initial conditions for the model in future efforts. Also, the problem of the over excitation of diurnal continental shelf waves needs to be addressed. The over excitation may be linked to the lack of alongshore mean currents in the model. Two improvements to the model that are presently in progress are 1) addition of the wind-induced mean circulation, and 2) coupling to the dynamic sea ice model of Tremblay & Mysak (1997). These improvements, along with improved hydrography, may alleviate the excessive continental shelf wave excitation. Inclusion of more of the forcing factors and dynamics will improve the model estimations. Furthermore, it is planned to investigate what the effects of tides are on surface pack ice, heat transfer to the atmosphere, and mixing in future efforts.

References

BAINES, P.G. 1974. The generation of internal tides over steep continental shelves. *Philosophical Transactions of the Royal Society, London*, **277**, 27–58.

BRINK, K.H. 1991. Coastal-trapped waves and wind-driven currents over the continental shelf. *Annual Review of Fluid Mechanics*, **23**, 389–412.

CUMMINS, P.F. & OEY, L.-Y. 1997. Simulation of barotropic and baroclinic tides off northern British Columbia. *Journal of Physical Oceanography*, **27**, 762–781.

DEACON, G.E.R. 1937. The hydrology of the Southern Ocean. *Discovery Reports*, **15**, 1–124.

DOAKE, C.S.M. 1992. Gravimetric tidal measurements on Filchner Ronne Ice Shelf. *Filchner Ronne Ice Shelf Programme Report*, No. 6, 34–39.

EGBERT, G.D. & EROFEEVA, S.Y. 2002. Efficient inverse modeling of barotropic ocean tides. *Journal of Atmospheric and Oceanic Technology*, **19**, 22 475–22 502.

FOREMAN, M.G.G. 1977. *Manual for tidal height analysis and prediction.* Pacific Marine Science Report No. 77–10. Patricia Bay, Sidney, BC: Institute of Ocean Sciences, 58 pp.

FOREMAN, M.G.G. 1978. *Manual for tidal current analysis and prediction.* Pacific Marine Science Report No. 78–6. Patricia Bay, Sidney, BC: Institute of Ocean Sciences, 70 pp.

GARRETT, C. 2003. Internal tides and ocean mixing. *Science*, **301**, 1858–1859.

GEIGER, C.A., ACKLEY, S.F. & HIBLER III, W.D. 1998. Sea ice drift and deformation processes in the western Weddell Sea. *Antarctic Research Se*ries, **74**, 141–160.

GOURETSKI, V.V. & JANCKE, K. 1999. A description and quality assessment of the historical hydrographic data for the South Pacific Ocean. *Journal of Atmospheric and Oceanic Technology*, **16**, 1791–1815.

HAIDVOGEL, D.B., WILKIN, J.L. & YOUNG, Y. 1991. A semispectral primitive equation circulation model using vertical sigma and orthogonal curvilinear horizontal coordinates. *Journal of Computational Physics*, **94**, 151–185.

HELLMER, H.H. & OLBERS, D.J. 1989. A two-dimensional model for the thermohaline circulation under an ice shelf. *Antarctic Science*, **4**, 325–326.

HUTHNANCE, J.M. 1989. Internal tides and waves near the continental shelf edge. *Geophysical and Astrophysical Fluid Dynamics*, **48**, 81–106.

HUTHNANCE, J.M. 1978. On coastal trapped waves: analysis and numerical calculation by inverse iteration. *Journal of Physical Oceanography*, **8**, 74–92.

LYTHE, M.B., VAUGHAN, D.G. & the BEDMAP CONSORTIUM. 2000. BEDMAP - bed topography of the Antarctic. 1:10 000 000 scale map. *BAS (Misc)* 9. Cambridge: British Antarctic Survey.

MIDDLETON, J.H., FOSTER, T.D. & FOLDVIK, A. 1982. Low-frequency currents and continental shelf waves in the southern Weddell Sea. *Journal of Physical Oceanography*, **12**, 618–634.

MUNK, W. & WUNSCH, C. 1998. The moon and mixing: abyssal recipes II. *Deep-Sea Research*, **45**, 1977–2010.

PADMAN, L., FRICKER, H.A., COLEMAN, R., HOWARD, S. & EROFEEVA, L. 2002. A new tide model for the Antarctic ice shelves and seas. *Annals of Glaciology*, **34**, 247–254.

Pereira, A.F., Beckmann, A. & Hellmer, H.H. 2002. Tidal mixing in the southern Weddell Sea: results from a three-dimensional model. *Journal of Physical Oceanography*, **32**, 2151–2170.

Robertson, R. 2005. Baroclinic and barotropic tides in the Ross Sea. *Antarctic Science*, **17**, 107–120.

Robertson, R. 2001a. Internal tides and baroclinicity in the southern Weddell Sea: Part I: Model description, and comparison of model results to observations. *Journal of Geophysical Research*, **106**, 27001–27016.

Robertson, R. 2001b. Internal tides and baroclinicity in the southern Weddell Sea: Part II: Effects of the critical latitude and stratification. *Journal of Geophysical. Research*, **106**, 27017–27034.

Robertson, R., Beckmann, A. & Hellmer, H. 2003. M_2 tidal dynamics in the Ross Sea. *Antarctic Science*, **15**, 41–46.

Robertson, R., Padman, L. & Egbert, G.D. 1998. Tides in the Weddell Sea. *Antarctic Research Series*, **75**, 341–369.

Robinson, A.V. & Makinson, K. 1992. Preliminary results from hot water drilling and oceanographic measurements under Ronne Ice Shelf. *Filchner Ronne Ice Shelf Programme Report*, No. 6, 340–46.

Shchepetkin, A. & McWilliams J.C. 2003. A method for computing horizontal pressure gradient force in an oceanic model with a non-aligned vertical coordinate. *Journal of Geophysical Research*, **108**, doi: 10.1029/2001JC001047.

Smith, W.H.F. & Sandwell, D.T. 1997. Global seafloor topography from satellite altimetry and ship depth soundings. *Science*, **277**, 1956–1962.

Smithson, M.J., Robinson, A.V. & Flather, R.A. 1996. Ocean tides under the Filchner–Ronne Ice Shelf, Antarctica. *Annals of Glaciology*, **23**, 217–225.

Song, Y. & Haidvogel, D.B. 1993. Numerical simulations of CCS under the joint effect of coastal geometry and surface forcing. *In* Spaulding, M.L. *et al*., *eds*. *Estuarine and Coastal Modeling*, *3rd International Conference*. Chicago, IL: ASCE, 216–243.

Song, Y. & Haidvogel, D.B. 1994. A semi-implicit ocean crculation model using a generalized topography-following coordinate. *Journal of Computational Physics*, **115**, 228–244.

Tremblay, L.-B. & Mysak, L.A. 1997. Modeling sea ice as a granular material, including the dilatancy effect. *Journal of Physical Oceanography*, **27**, 2342–2360.

Umlauf, L. & Burchard, H. 2003. A generic length-scale equation for geophysical turbulence. *Journal of Marine Research*, **61**, 235–265.